Dalton Transactions

ROYAL SOCIETY OF CHEMISTRY

PAPER

View Article Online
View Journal | View Issue

Check for updates

Cite this: *Dalton Trans.*, 2025, **54**, 6117

Heterometallic CuCd and Cu_2Zn complexes with *o*-vanillin and its Schiff-base derivative: slow magnetic relaxation and catalytic activity associated with Cu(II) centres†

Olga Yu. Vassilyeva, *[a] Oksana V. Nesterova, *[b] Alina Bieńko, [c]
Urszula K. Komarnicka, [c] Elena A. Buvaylo,[a] Svitlana M. Vasylieva,[d]
Brian W. Skelton[e] and Dmytro S. Nesterov *[b]

Received 29th December 2024,
Accepted 6th March 2025

DOI: 10.1039/d4dt03571b

rsc.li/dalton

In this work, two novel heterometallic mixed-ligand mixed-anion complexes $[Cu^{II}Cd^{II}ClL(o\text{-}Van)(OAc)]\cdot 3H_2O$ (**1**) and $[Cu^{II}_2Zn^{II}Cl_2L_2(o\text{-}Van)(OAc)]$ (**2**) were prepared by reacting fine copper powder and Cd(II) or Zn(II) acetate with an ethanol solution of the Schiff-base ligand HL formed *in situ* in the condensation reaction of 2-hydroxy-3-methoxy-benzaldehyde (*o*-VanH) and $CH_3NH_2\cdot HCl$. The compounds were thoroughly characterized by elemental analysis, FT-IR, UV/Vis and EPR spectroscopy, cyclic voltammetry, and single-crystal X-ray diffraction, revealing the neutral molecular nature of both the compounds. Catalytic properties of **1** and **2** were studied in the oxidation of hydrocarbons with H_2O_2 under mild conditions, showing the maximum reaction rate of 4×10^{-5} M s^{-1} and TOF up to 640 h^{-1}. Both compounds undergo complex transformations in solution as evidenced by kinetic analysis and time-dependent UV/Vis spectroscopy, indicating that the reduced Cu(I) form of **1** is unexpectedly unfavorable. Complex **1** demonstrates slow magnetic relaxation dominated by the direct relaxation process between T = 1.8 and 7 K under an external DC field of 0.2 and 0.4 T, a very rarely observable effect in the coordination compounds of Cu(II). Complex **2** possesses weak ferromagnetism (J = 4.50 cm^{-1}, zJ' = −0.201 cm^{-1} for $H = -JS_1S_2$ formalism) occurring through the Cu–O–Cu pathways. Theoretical CASSCF, DFT and TDDFT calculations were applied to investigate the electronic structures of **1** and **2** and rationalize their behavior in solution.

Introduction

Natural metal-containing enzymes such as the cytochrome P450 or methane monooxygenase (MMO) families play a crucial role in biological systems, serving as versatile catalysts in the oxidation of unactivated C–H bonds of various organic substrates.[1–4] The ability to mimic these enzymatic processes continues to attract considerable research interest in the development of metal complexes with analogous catalytic properties.[2] Coordination compounds of copper attract special attention in this field due to the high occurrence of copper-mediated enzymatic processes. Furthermore, copper is a cheap, abundant 3d metal whose compounds typically possess low toxicity to higher living organisms.[5] The catalytic properties of copper compounds are associated with the ability of copper to participate in several stable oxidation states, which can be interconverted with low overpotential. This property is particularly important for catalytic cycles that are highly involved in redox processes. These features stipulate the broad applications of copper-based catalysts in contemporary catalysis and preparative organic chemistry.[5–7]

Careful tuning of the properties of a copper catalyst could be achieved through the creation of a specific coordination environment as well as the incorporation of a closely located metal centre of different kind. The pronounced influence of the second redox-inactive metal on the main catalytic centre

---

[a] *Department of Chemistry, Taras Shevchenko National University of Kyiv, 64/13 Volodymyrska Str., Kyiv 01601, Ukraine. E-mail: vassilyeva@univ.kiev.ua*

[b] *Centro de Estudos de Engenharia Química, Instituto Superior de Engenharia de Lisboa, Instituto Politécnico de Lisboa, R. Conselheiro Emídio Navarro, 1, 1959-007 Lisboa, Portugal. E-mail: oksana.nesterova@vis.isel.pt, dmytro.nesterov@vis.isel.pt*

[c] *Faculty of Chemistry, University of Wroclaw, 47 Joliot Curie, 50-137 Wroclaw, Poland*

[d] *National Technical University of Ukraine "Igor Sikorsky Kyiv Polytechnic Institute", 37 Beresteiskyi Ave., Kyiv 03056, Ukraine*

[e] *School of Molecular Sciences, M310, University of Western Australia, Perth, WA 6009, Australia*

† Electronic supplementary information (ESI) available: Experimental protocols, IR and EPR spectra, crystallographic bonds and angles, figures of the DFT optimized structures, listings of the calculations output and cartesian atomic coordinates. CCDC 1958659 1960155. For ESI and crystallographic data in CIF or other electronic format see DOI: **https://doi.org/10.1039/d4dt03571b**

(synergic effect of dissimilar metals) has been demonstrated in many artificial examples, where the second metal stabilizes the uncommon oxidation state of the redox-active 3d metal.[8] Prominent examples include the stabilization of the Co^{IV} high-valent metal-oxo species[9,10] or activation of manganese-oxo clusters[11] by the presence of redox-inactive metal ions. Some of us have reported on the effect of a pronounced enhancement of the catalytic activity for $Co^{III}Cd^{II}$ and $Co^{III}Zn^{II}$ catalysts[12,13] in comparison to the parent Co^{III} complex in the mild hydroxylation of sp^3 C–H bonds with organic peroxides. The synergic catalytic effect of the heterometallic complexes is also recognized for the case where the second metal is also redox-active, but has properties different from those of the main metal. For instance, this effect was manifested by the $Co_4^{III}Fe_2^{III}$ Schiff-base compound, which revealed an exceptionally high catalytic activity in the oxidation of C–H bonds with H_2O_2 or *m*-chloroperoxybenzoic acid.[14,15] Thus, heterometallic catalysts have found numerous applications in chemistry, providing the catalytic parameters that are hardly achievable for homometallic catalysts.[16,17]

In our ongoing research, we focus on the design of heterometallic complexes, exploring new combinations of metal centres and ligands to unravel the intricate factors that govern their catalytic behavior and other functional properties.[12,15,18–20] The formation of polymetallic cores induces the appearance of magnetic coupling and redox-interactions between the bridged paramagnetic centres, and an examination of the exchange interactions is a necessary routine in the search for new findings.[20,21] The principal feature of this synthetic pathway towards heterometallic complexes is the use of a zerovalent metal powder with another metal salt in their reaction with a non-aqueous solution of a proton-donating ligand in air.[19,22] Dioxygen from the air is reduced to give H_2O, the only by-product of the interaction. This strategy resulted in many 3d/3d and 3d/4d heterobimetallic and 3d/3d/3d heterotrimetallic compounds with fascinating structures and properties.[18,23–27]

In the present work, two novel heterometallic mixed-ligand mixed-anion complexes [CuCdClL(*o*-Van)(OAc)]·3H_2O (**1**) and [$Cu_2ZnCl_2L_2$(*o*-Van)(OAc)] (**2**) (Scheme 1) were prepared by reacting a fine copper powder and Cd(II) or Zn(II) acetate with a methanol solution of the Schiff-base ligand HL formed *in situ* from 2-hydroxy-3-methoxy-benzaldehyde (*o*-vanillin, *o*-VanH) and CH_3NH_2·HCl. The catalytic performance of complexes **1** and **2** in the hydroxylation of a series of hydrocarbons with H_2O_2 as an oxidant under mild conditions in the presence of various promoters was examined. Direct current (DC) and alternating current (AC) magnetic susceptibility measurements provided clear evidence of a field-supported slow magnetic relaxation of complex **1** at low temperature. Theoretical DFT and CASSCF calculations provided useful insights into the electronic properties, magnetic interactions, and catalytic reaction pathways for the analysed compounds.

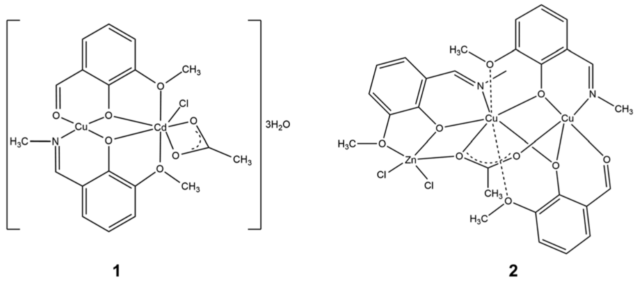

1

2

Scheme 1 Structural formulas of [CuCdClL(*o*-Van)(OAc)]·3H_2O (**1**) and [$Cu_2ZnCl_2L_2$(*o*-Van)(OAc)] (**2**).

Results and discussion

Synthesis and IR spectroscopic characterization

Based on the previous successful experience of obtaining heterometallic Co^{III}/M^{II} (M^{II} = Mn, Co, Cd, Zn) complexes with the HL ligand using a salt of one metal and a powder of another with free access to air oxygen,[12,13,28,29] copper powder and Zn or Cd salts were used as a source of metals for the syntheses of complexes **1** and **2** (see ESI† for details). The use of methylamine hydrochloride instead of a conventional aqueous solution of the amine in the *in situ* ligand preparation led to the appearance of chloride anions in the reaction media competing with the acetate groups of the metal salt. The reaction conditions favour partial amine-aldehyde condensation, yielding a combination of two kinds of aromatic ligands in both compounds.

The elemental analysis and IR spectroscopy data agree with the presence of both deprotonated *o*-vanillin and HL ligands in **1** and **2**. The characteristic vibrations of both Schiff-base HL ($\nu_{C=N}$ 1634 cm^{-1}, $\nu_{Ar\text{-}OH/OCH_3}$ 1254 cm^{-1}) and *o*-vanillin ($\nu_{C=O}$ 1640 cm^{-1}, $\nu_{Ar\text{-}OH/CH_3}$ 1258 cm^{-1}) are clearly observed in the spectra of **1** and **2** in the respective regions (Fig. S1†). Acetate groups are identified in the spectra of **1** (ν_{as} 1612 cm^{-1}, ν_s 1462 cm^{-1}) and **2** (ν_{as} 1615 cm^{-1}, ν_s 1465 cm^{-1}) as the most intense absorptions, partially overlapping with the deprotonated iminophenol and *o*-vanillin bands.

Crystal structures

Compound **1** crystallizes in the triclinic space group $P\bar{1}$ (Table S1†); the neutral molecule contains two metal centres, the deprotonated Schiff-base and *o*-vanillin ligands, as well as acetate and chloride ligands (Fig. 1, top). The Cu⋯Cd pair of metals is bridged by two phenolate μ-O atoms from the two ligands, resulting in the metal–metal separation of 3.395 Å. Major part of the molecule, except for the coordinated Cl atom and the acetate group, is essentially planar. The coordination around the Cu atom is square planar with the Cu–N/O bond lengths falling in the range of 1.9095(19)–1.937(2) Å, the *cis* bond angles at the metal atom varying from 81.62(8)° to 93.05(9)°, and the *trans* angles approaching 175° (Table S2†). The Cd atom is seven-coordinate, adopting a distorted pentagonal bipyramid environment, with the Cd–O distances ranging from 2.3136(18) Å to 2.5377(19) Å, and a Cd–Cl separation of 2.4773(8) Å (Table S2†). The bond angles at the metal atom vary in the range 64.78(6)°–164.54(7)°. The hydrogen bonds formed by the uncoordinated water molecules in the structure

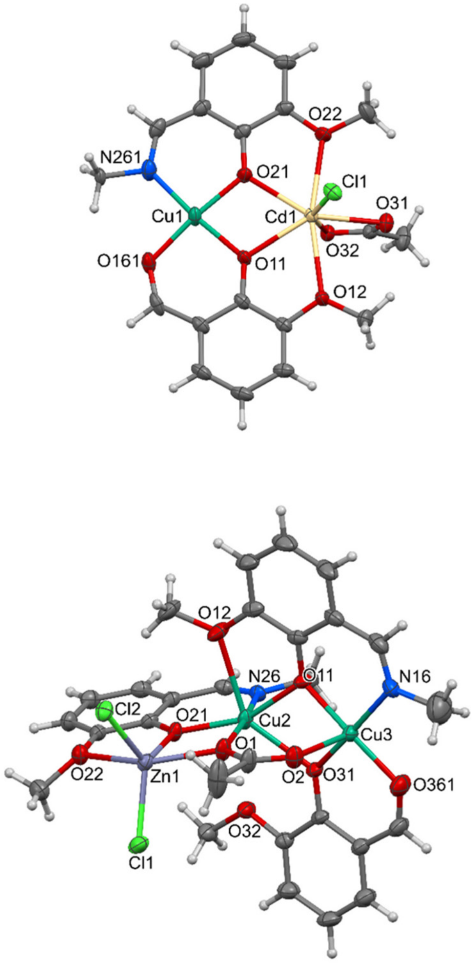

Fig. 1 Molecular structures and principal labelling of [CuCdClL(*o*-Van)(OAc)]·3H_2O (**1**) (top) and [$Cu_2ZnCl_2L_2$(*o*-Van)(OAc)] (**2**) (bottom) with ellipsoids at the 50% probability level.

of **1** join the heterometallic assemblies into a 1D H-bonded chain along the *a*-axis (Fig. S2a and Table S3†).

Compound **2** crystallizes in the orthorhombic space group $Pca2_1$ (Table S1†); the neutral molecule contains three metal centres, two deprotonated Schiff-base ligands, one deprotonated *o*-vanillin, one acetate and two chloride ligands (Fig. 1, bottom). Each pair of metals (Cu⋯Cu and Zn⋯Cu) is bridged by two μ-O atoms from two ligands. The deprotonated *o*-vanillin and one L^- ligand link the two copper atoms, and the other deprotonated Schiff base and the acetate group bridge the Cu⋯Zn pair, enabling the metal–metal separations of 3.123 Å and 3.167 Å, respectively. The coordination polyhedron around the zinc centre can be viewed as a distorted square pyramid. The distance to the axial methoxy oxygen atom, *d*(Zn1–O22) = 2.398(3) Å, is significantly longer than those to the other ligands; the mean of the two other Zn–O and two Zn–Cl bond distances are equal to 2.078 Å and 2.227 Å, respectively (Table S4†). The *cis* bond angles at the Zn atom vary from 72.17(11)° to 126.23(5)°, and the *trans* O1–Zn1–O22 angle is 146.43(11)°. The copper atom Cu2 in the structure of **2** is heptacoordinate with the five Cu–O/N bond distances lying in the range from 1.944(3) Å to 2.291(2) Å, and the two long contacts Cu⋯O12 and Cu⋯O32 constituting 2.505(3) Å and 2.916(3) Å, respectively (Table S4†). The existence of these weak contacts is obvious from the point of view of saturation of the coordination environment of the Cu2 centre. Also, the analysis of the electron density in terms of the Quantum Theory of Atoms in Molecules (QTAIM)[30,31] revealed the presence of the bond critical points (BCP, Fig. S3†) of the long contacts Cu⋯O12 and Cu⋯O32 with the electron densities $\rho(r_{\text{BCP}})$ of 0.025 a.u. and 0.011 a.u., respectively. The bond angles at the metal atom vary from 59.23(10)° to 171.44(14)° (Table S4†). The coordination about Cu3 is almost a regular square pyramid with the four basal Cu–N/O bond lengths falling in the range of 1.935(3)–1.966(4) Å and the fifth apical bond Cu3–O2 at 2.260(3) Å to the acetate oxygen being strongly elongated (Fig. 1, bottom; Table S4†). The bond angles at the metal atom vary from 83.01(13)° to 172.58(17)°. In the crystal structure, the trinuclear molecules of **2** related by a 2-fold rotation axis are stacked parallel to the *ac* plane (Fig. S2b†). The minimal metal–metal distance of 7.7865(9) Å in the lattice is between the Zn1 and Cu2 atoms of the adjacent molecules in a stack. The weak C–H⋯Cl hydrogen bonding (Table S3†) consolidates the extended supramolecular 3D network structure.

Cyclic voltammetry

The electrochemical features of **1** and **2** were probed by cyclic voltammetry in methanol solutions in the potential range from +1.0 to −1.0 V. The cyclic voltammograms (CV) are given in Fig. S4.† The anodic scans, starting from the open circuit potential (0.03 and 0.25 V *vs.* Ag/AgCl for **1** and **2**, respectively), display clear irreversible oxidation peaks at +0.73 V for both compounds. A similar behavior was observed in the case of the electrochemical response of the Fe(iii) complex with *o*-vanillin [FeCl(*o*-Van)$_2$(H_2O)] measured in the same conditions, where the irreversible peak at +0.71 V in the anodic scan was associated with the oxidation of the *o*-vanillin ligand.[32] In the CVs of both complexes, the ill-defined oxidation waves at $E_{\text{pa}} \sim +0.42$ V coupled with corresponding reduction waves at $E_{\text{pc}} \sim +0.40$ V (demonstrating the non-equivalent current intensity of the cathodic and anodic peaks) indicate a quasi-reversible redox process which can be related to the L^- ligand. During the first cycle, in the backward scans, the reduction of Cu^{2+} to Cu^0 occurs at potentials lower than −0.40 V and is followed by a re-oxidation process at 0.033 (**1**) and 0.045 V (**2**). The reduction from Cu^{2+} to Cu^0 is superimposed with the solvent reduction peak evidenced by comparing the CVs of the complexes and supporting electrolyte solutions in methanol (Fig. S5†), while the reduction to Cu^{1+} is not observed. This finding may be due to the presence of acetate ions in **1** and **2**, as it was reported that the Cu^{2+}/Cu^+ redox process was not observed for the copper(ii) acetate complex with the bis(3,5-dimethylpyrazol-1-yl)methane ligand (L^1).[33] During the anodic scan of the CV of **1**, a shoulder at −0.036 V is detected, which evolves into a separate peak in further cycles. The origin of the related oxidation process was not recognized.

EPR spectroscopy

The polycrystalline X-band EPR spectra of the magnetically concentrated samples of **1** and **2** were recorded at different temperatures (298 and 77 K). The spectra show a typical axial pattern with no resolved hyperfine structure (Fig. S6,† top). There is no change in the line shape, line width and resolution as a function of temperature for both complexes; no half-field signal is observed. The X-band EPR spectrum for **2** does not provide any evidence of Cu(II)–Cu(II) interaction. The anisotropic EPR spectral features can be associated with the axial symmetry having $d_{x^2-y^2}$ ground state with the square planar, square pyramidal or elongated octahedral geometry of the copper polyhedron (the ground state was confirmed by the theoretical studies, see below). The observed g values $g_x = g_y = 2.055$, $g_z = 2.20$ ($g_{av} = 2.106$) for **1** and $g_x = g_y = 2.057$, $g_z = 2.28$ ($g_{av} = 2.131$) for **2** agree with the observed distorted coordination environment of copper(II) ions in both complexes. The X-band spectrum of the frozen solution of **1** in DMF demonstrates the same symmetry where the hyperfine structure arising from the interaction with a copper nucleus is clearly seen (Fig. S7†). The simulation of the spectrum resulted in g-factors close to those obtained for the solid samples, confirming the preservation of the structure of **1** in solution.

The room temperature Q-band EPR spectrum of **2** is shown in Fig. S6,† bottom, where the strong transition at 8000 G confirms the ferromagnetic behaviour of the compound. The respective signal can be understood as an unresolved absorbance from $\Delta M_s = 2$ transition. A similar broadening effect of the EPR spectra of the copper dimeric system was observed earlier.[34] The spectra show axial symmetry similar to that observed in the X-band region.

Magnetic measurements

DC magnetic measurements

The molar magnetic susceptibility for complex **1** has been converted to the $\chi_M T$ product whose temperature dependence is displayed in Fig. 2, top left. The field dependence of the magnetization per formula unit $M_1 = M_{mol}/N_A\mu_B$ at constant temperature is shown in Fig. 2, bottom left.

Given the diamagnetic character of Cd(II) ions, from a magnetic point of view, complex **1** can be considered a monomeric compound. The product function $\chi_M T$ (and/or the effective magnetic moment) for **1** (Fig. 2, top left) systematically decreases on cooling from room temperature down to T = 25 K; $\chi_M T$ (300 K) = 0.47 cm^3 mol^{-1} K ($\mu_{eff} = 1.92\mu_B$) is slightly higher than the spin-only value of 0.37 cm^3 mol^{-1} K ($1.73\mu_B$) calculated for Cu^{II} (with $S = {}^1/_2$ and $g_{av} = 2.00$). Below 25 K, a rapid decrease of the $\chi_M T$ product is observed up to $\chi_M T$ (1.8 K)

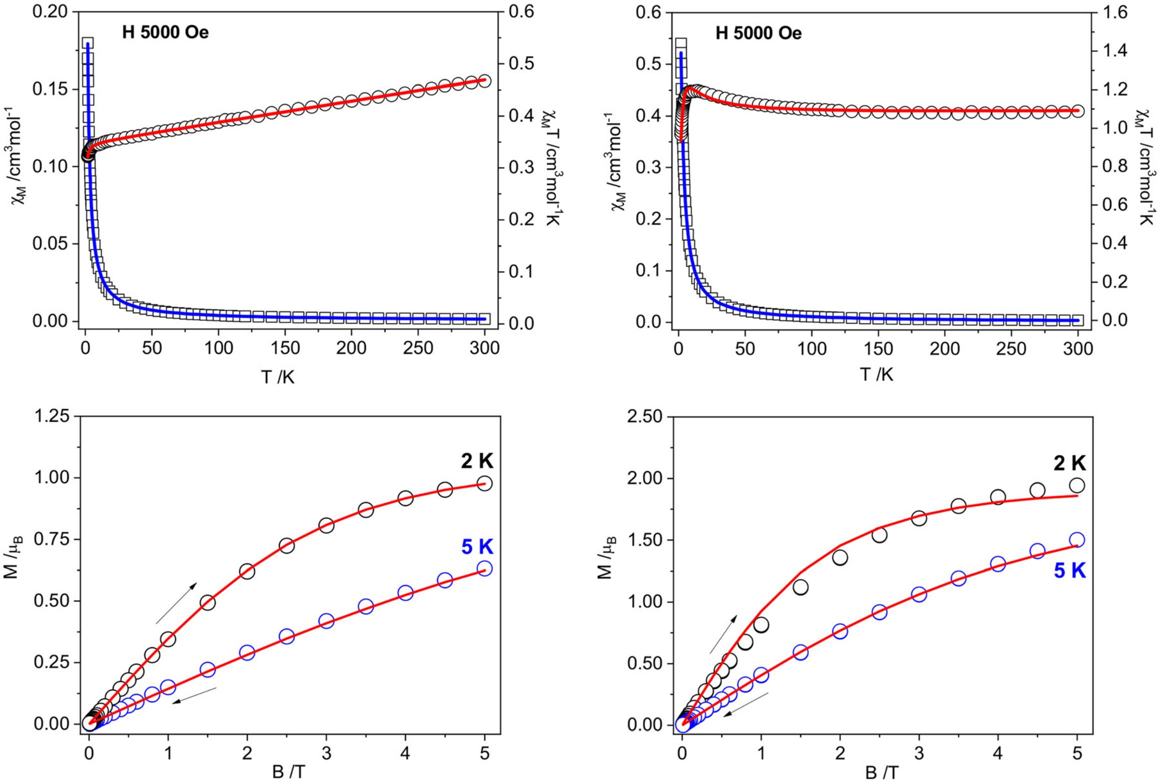

1

2

Fig. 2 DC magnetic data for **1** and **2**. Top: temperature dependences of the χ_M (squares) and $\chi_M T$ (circles). Bottom: field dependences of the magnetization per formula unit. The solid lines (on both graphs) are calculated using the PHI program.[35]

= 0.32 cm^3 mol^{-1} K (1.61μ_B). The magnetic features indicate rather weak antiferromagnetic exchange interactions. A significant contribution of the temperature-independent paramagnetism (TIP) is reflected in the slope of the $\chi_M T$ dependency at higher temperatures. At 2.0 K and 5 T magnetization per formula unit, $M_1 = M_{mol}/N_A\mu_B$ reaches the maximum value of $M_s = 0.98\mu_B$ (Fig. 2, bottom left), which is adequate for the ground state $S = {}^1/_2$.

The fitting of the magnetic data of **1** [simultaneous fitting of $\chi T(T)$ and $M(H)$ dependences] was carried out using the PHI program for the $S = \frac{1}{2}$ spin state,[35] considering various Cu⋯Cu intermolecular interactions transmitted through hydrogen bonds, described by the effective zJ' parameter (where z is the number of adjacent paramagnetic species around a given copper centre). The TIP was also included in the fitting procedure. The best agreement with the experimental magnetic data for **1** was obtained with $zJ' = -0.1$ cm^{-1}, $g = 2.09$, and TIP = 407 × 10^{-6} cm^3 mol^{-1}, $R = \sum[(\chi T)\text{exp} - (\chi T)\text{calc}]^2/\sum[(\chi T)\text{exp}]^2 = 7.1 \times 10^{-5}$ (solid lines in Fig. 2, left). The value of the zJ' parameter is consistent with a very weak antiferromagnetic character of **1** due to a long distance between the nearest Cu(II) ions in the crystal lattice (6.06 Å). The correctness of the obtained results was confirmed by alternative calculations using a susceptibility equation (eqn (1)) with a molecular field correction (eqn (2)) (Fig. S8†).

The least squares fit of the experimental data by these expressions leads to the following parameters: g_{av}(Cu) = 2.09 and $zJ' = -0.102$ cm^{-1}, TIP = 406 × 10^{-6} cm^3 mol^{-1}, $R = 6.21 \times 10^{-5}$.

$$\chi_M = \frac{g^2 N\beta^2}{3kT} S(S+1) \tag{1}$$

$$\chi'_M = \frac{\chi_M}{1 - \left(\frac{2zJ'}{N\beta^2 g^2}\right)\chi_M} \tag{2}$$

The TIP value is notably higher than the established value of 60 × 10^{-6} cm^3 mol^{-1} for Cu(II) compounds. Since the repeated magnetic measurements using two different SQUID (MPMS and MPMS3) magnetometers showed the same result, the possibility of the slope of the χT plot being an experimental issue was ruled out. Although the origin of the observed phenomenon remains unclear, it is known in the literature for several metal ions. In the case of copper(II) complexes, TIP values as high as 309 × 10^{-6},[36] 360 × 10^{-6},[37] and 413 × 10^{-6} cm^3 mol^{-1} (ref. 36) have been previously reported.

In the case of **2**, the $\chi_M T$ value (or magnetic moment) [per two Cu(II) centres] *vs.* temperature shows an increase from 1.09 cm^3 mol^{-1} K (2.95μ_B) at 300 K to 1.19 cm^3 mol^{-1} K (3.09μ_B) at 8.0 K (Fig. 2, top right). Below this temperature, the $\chi_M T$ product decreases down to 0.97 cm^3 mol^{-1} K (2.78μ_B) at 1.8 K. This magnetic feature evidences the presence of ferromagnetic exchange coupling between two Cu(II) ions ($S_A = S_B = \frac{1}{2}$) that can be described by the model of binuclear units, together with various additional Cu⋯Cu intermolecular interactions transmitted through hydrogen bonding (zJ' parameter). The calculations were based on the Heisenberg–Dirac–Van Vleck Hamiltonian in zero field given by eqn (3)

$$\hat{H} = -J\hat{S}_A\hat{S}_B - zJ'\langle S_z\rangle\hat{S}_z \tag{3}$$

using the PHI program (simultaneous fitting of $\chi T(T)$ and $M(H)$ dependences). The TIP was also included into the fitting procedure. The best agreement with the experimental magnetic data for **2** was obtained with $J = 4.50$ cm^{-1}, $zJ' = -0.201$ cm^{-1}, $g = 2.18$, TIP = 68 × 10^{-6} cm^3 mol^{-1}, $R = \Sigma[(\chi T)\text{exp} - (\chi T)\text{calc}]^2/\sum[(\chi T)\text{exp}]^2 = 2.1 \times 10^{-7}$ (red lines in Fig. 2, right). The calculated curve matches the magnetic data well. The maximum value of magnetization [per formula unit $M_1 = M_{mol}/(N_A\mu_B)$] at $B = 5$ T and $T = 2.0$ K of 1.94μ_B is very close to the saturation value expected for the $S = 1$ ground state (Fig. 2, bottom right). The magnetic data clearly confirm the weak ferromagnetic character of complex **2**.

The explanation of these properties fits into the theories presented so far.[36–40] For dimers with planar or near planar Cu_2O_2 cores, this weak ferromagnetic interaction present in complex **2** is a result of an interplay of several structural parameters: the two differing Cu–O–Cu angles, φ = 94.91° and 103.26° (for $\varphi > 97.5°$, the interaction is predicted to be antiferromagnetic, $S = 0$ ground state; and for $\varphi < 97.5°$, the ground state is $S = 1$ and the interaction should be ferromagnetic), the Cu⋯Cu distance of 3.123 Å, and the dihedral distortion angle between the two CuO_2 planes of the LCu(μ-O)$_2$Cu(*o*-Van) fragment (δ = 155.4°) being far from 180° (a typical value for strong antiferromagnetic interaction). Moreover, the presence of an additional exchange path through the acetate bridge may reduce the strength of ferromagnetic interactions. However, the appreciable intensity of the intermolecular interaction (zJ') in **2** may indicate the presence of a non-negligible second exchange pathway within the compound, which can be attributed to non-covalent bonding in the crystal lattice.

AC susceptibility

AC susceptibility data were acquired first at $T = 2.0$ K for a set of representative frequencies of the alternating field (f = 1.0, 11, 1111, and 1116 Hz) by ramping the magnetic field from zero to $B_{DC} = 0.5$ T or even higher; the working amplitude $B_{AC} = 0.3$ mT was used. For both complexes, there is no absorption signal (out-of-phase susceptibility component χ'') at the zero magnetic field owing to the fast magnetic tunnelling. In the case of **1**, the out-of-phase susceptibility χ'' increases with the applied field up to a maximum, and is then attenuated (Fig. 3). This graph shows the regions in which individual frequencies yield the maximum response, and indicates that **1** can exhibit the field-induced slow magnetic relaxation.

The next scans of the mapping magnetic response were performed at a fixed external magnetic field B_{DC} = 0.2 and 0.4 T, changing the frequency between f = 0.1 to 1500 Hz for a set of temperatures between T = 1.8 and 7 K (Fig. 4). The out-of-phase susceptibility curve shows a well-developed peak at 2 K

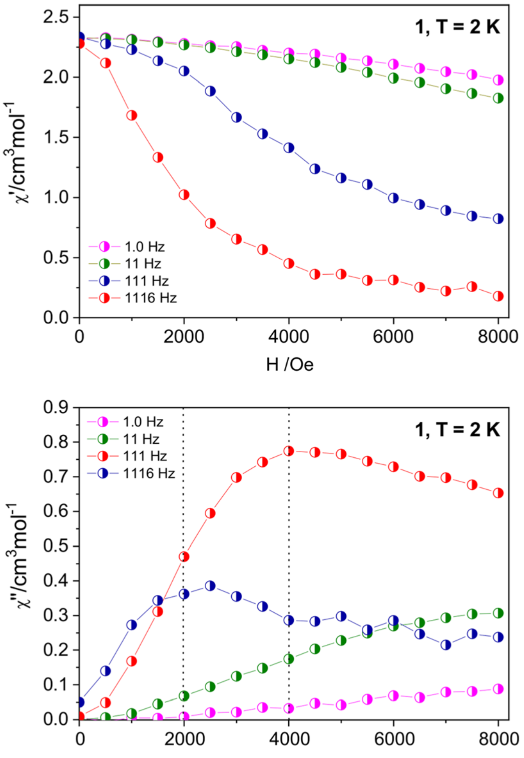

Fig. 3 Field scan of the AC susceptibility for **1** at T = 2.0 K for four trial frequencies. Vertical marks indicate the frequencies selected for a detailed mapping. Lines – visual guide.

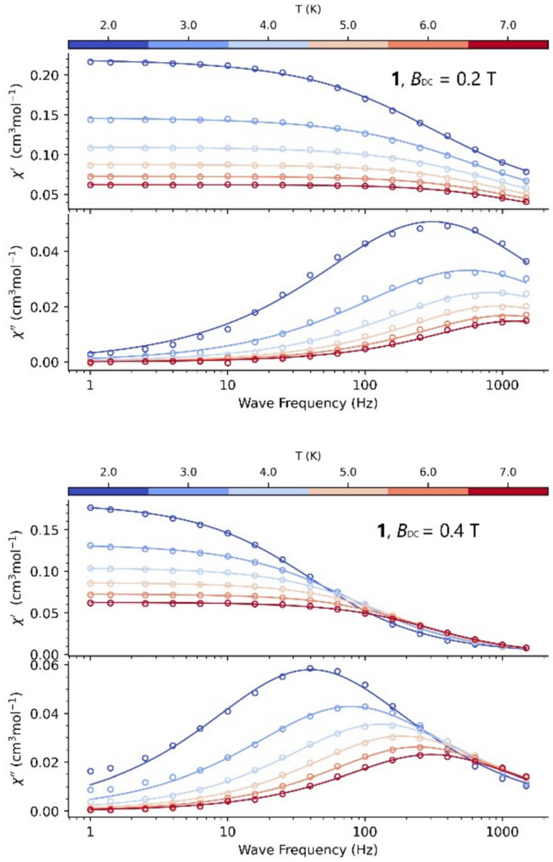

Fig. 4 Frequency scan of the AC susceptibility for **1** at fixed B_{DC} for varied T. Lines – fitted.

and B_{DC} = 0.2 T with the maximum lying at f = 350 Hz. With increasing external field (B_{DC} = 0.4 T), the peak at the χ'' *vs.* f function moves to lower frequencies around 80 Hz at T = 2.0 K. The AC susceptibility data were fitted using CC-FIT2 software[41] by employing the Generalized Debye model (appropriate if the experimental Argand diagram can be recovered using a small value of the parameter α, *i.e.*, $0 \leq \alpha \leq 1$) (Fig. 4, S9;† Tables S5, S6†). The experimental curves without maxima were omitted. The fitting procedure gave the value of the relaxation time at 2 K equal $\tau = 5.17 \times 10^{-4}$ s at 0.2 T and $\tau = 3.95 \times 10^{-3}$ s at 0.4 T. Upon heating, the relaxation time decreases as expected to $\tau = 1.29 \times 10^{-4}$ s at 0.2 T and $\tau = 5.28 \times 10^{-4}$ s at 0.4 T and T = 7.0 K.

Fig. S10† shows the temperature dependence of the relaxation rates, which can be converted to the relaxation time using equation $\tau^{-1} = \exp(-\{\ln(\tau)\})$. A fit to the linear function was used in determining the direct-process parameters, proceeding according to the formula $\tau^{-1}(T) = 10^D T$, where D is equal to $\log_{10}[\mathrm{s}^{-1}\ \mathrm{K}^{-1}]$. The exponent $D = 3.057 \log_{10}[\mathrm{s}^{-1}\ \mathrm{K}^{-1}]$ exceeded the limit expected for the direct relaxation processes. At B_{DC} = 0.4 T, the end part (above 5 K) of the $\ln \tau$ *vs.* $\ln T$ dependence does not follow a linear relationship. Fitting the entire data set is possible using two models: the direct relaxation process and Raman process according to the formula $\tau^{-1}(T) = 10^R T^n$, where R is equal $\log_{10}[\mathrm{s}^{-1}\ \mathrm{K}^{-1}]$. The linear fit gave n = 1.4, $R = 1.931 \log_{10}[\mathrm{s}^{-1}\ \mathrm{K}^{-1}]$ and $D = -6.11 \log_{10}[\mathrm{s}^{-1}\ \mathrm{K}^{-1}]$. The value of n favors the direct relaxation process.

Single molecule, as well as single ion magnetism, is not expected for Cu(II) complexes due to the low spin state $S = \frac{1}{2}$ and the absence of a barrier to the spin reversal: the axial zero-field splitting parameter D is undefined. The presence of a relaxation process in complex **1** can be caused by structural and geometry peculiarities of the Cu(II) environment. The chromophore around the copper centre is distorted due to the asymmetric O_3N environment of the ion, non-similar metal–ligand distances and angle values different from 90°. Such anisotropic systems showing at least two distinct $g_z \neq g_x$ values are clearly seen in the axial signal of the EPR spectra. Thus, magnetic anisotropy exists even in the absence of zero-field splitting. It is worth noting that SMMs were identified for a variety of Cr(II), Mn(III), Fe(III), Fe(II), Fe(I), Co(II) and Ni(II) systems.[42] Only four examples were found among the mononuclear Cu(II) complexes, most of which had pentacoordinate $[\mathrm{Cu(12\text{-}TMC)Cl}][\mathrm{B(C_6H_5)_4}]$ (12-TMC = 1,4,7,10-tetramethyl–1,4,7,10-tetraazacyclododecane)[43] or hexacoordinate $[\mathrm{Cu(pydca)(dmpy)}]\cdot 0.5\mathrm{H_2O}$[44] (pydca = pyridine-2,6-dicarboxylato, dmpy = 2,6-dimethanolpyridine) and $[\mathrm{CuLL'_2(H_2O)}]$ (L = 2,6-dimethanolpyridine and HL' = 3,5-dinitrobenzoic acid)[45] geometry around the Cu(II) ion.

Electronic structures and exchange couplings

The presence of a single paramagnetic atom in **1** (a copper centre) enabled the use of *Ab Initio* Ligand Field Theory (AILFT) calculations, which allow for purification of the valence d-orbitals of a metal centre, as implemented in the ORCA 5.0.4 software package (see ESI† for details).[46] The AILFT calculations were performed at the DKH-def2-SVP/DKH-def2-TZVPP (for Cu and surrounding atoms)/SARC-DKH-TZVP (for Cd)[47] level operated in the CAS(9,5) active space of the copper 3d-orbitals for the molecular structure $\mathbf{1}^{\mathrm{HOPT}}$ with the positions of the hydrogen atoms optimized at the PBE0/ma-def2-SVP level.[48,49] The unpaired electron is located at the $2b_{1g}$ $d_{x^2-y^2}$ orbital (Fig. S11, Listing S1†), as expected for the Cu(II) centre in a square-planar coordination environment. The remaining low-lying 3d orbitals are non-degenerate due to the asymmetric O_3N surrounding of the copper centre. Involvement of the 4d copper orbitals to give the CAS(9,10) active space does not have a pronounced influence on the relative energies of 3d orbitals.

The CASSCF/NEVPT2 AILFT construction of the *g*-matrix for the molecule of $\mathbf{1}^{\mathrm{HOPT}}$ (Fig. S11†) gave $g_x = 2.072$, $g_y = 2.076$ and $g_z = 2.348$. The same calculation performed for the inverted disordered *o*-Van$^-$ and L$^-$ ligands resulted in similar *g*-factors. The correct prediction of *g*-factors requires involvement of excitations from low-lying orbitals.[50] Thus, the present results follow the experimentally determined values ($g_x = g_y = 2.055$, $g_z = 2.20$) only to a limited extent.

Although the copper centres in the structure of **1** are separated at 6.062 Å and 6.100 Å, it is known that exchange coupling may exist even at such distances.[51] The magnitude of the long-range exchange interactions between the paramagnetic centres in $\mathbf{1}^{\mathrm{HOPT}}$ was evaluated through the broken symmetry (BS) DFT calculations, which provide a useful and straightforward mechanism for estimating the magnetic couplings in polynuclear systems.[52–54] The respective calculations at the B3LYP/def2-SVP (def2-TZVPP for copper atoms) level[47,55–57] using the crystallographic coordinates yielded $J = -0.12$ and -0.2 cm^{-1} for the $d(\mathrm{Cu\cdots Cu}) = 6.062$ and 6.100 Å pairs, respectively. The fragment constructed from three molecules of **1** with the "central" molecule copper atom replaced by the diamagnetic zinc one [$d(\mathrm{Cu\cdots Cu}) = 12.088$ Å] resulted in a negligible value of $J = 0.01$ cm^{-1}. The predicted long-range *J* couplings fit well with the experimentally obtained mean value of $zJ' = -0.1$ cm^{-1}.

The SA-CASSCF calculations of complex **2** were performed at the same level as for **1**, except for the absence of a SARC-DKH-TZVP basis set, which was applied for the cadmium atom in **1**. The $\mathrm{Cu^{II}(\mu\text{-}O)_2Cu^{II}}$ coordination core of $\mathbf{2}^{\mathrm{HOPT}}$ was oriented with the origin of coordinates placed between the copper centres, while the *x*- and *y*-axes are in the plane of the core. The CAS(18,10) calculation involving all 3d orbitals of both copper atoms (Fig. S12†) results in the triplet ground state with the first singlet state located just 5.8 cm^{-1} above it. The NEVPT2 correction resulted in an even lower gap of 3.8 cm^{-1}. Although CASSCF(NEVPT2) is expected to underestimate the exchange couplings due to the absence of excitations beyond the active space, it resulted in a good agreement in the present case with the experimentally observed singlet–triplet gap (4.50 cm^{-1}). The state-averaged calculation over the first 10 roots for the singlet and triplet multiplicities resulted in two groups of doubly-generate orbitals having e'' and e' symmetries, and a low-lying group of six orbitals with the energies being close to six-fold degeneration (Fig. S12†). The ground state of the molecule represents the single-reference triplet, where the unpaired electrons are located at the molecular orbitals representing the mixture of $d_{x^2-y^2}$ orbital of Cu3 and d_{z^2} orbital of Cu2 (72% contribution in total). Such distribution of the highest-energy 3d-orbitals is the outcome of the square-pyramidal coordination environment around Cu3 and the complex heptacoordinated sphere around Cu2 with rather short axial Cu–O(N) distances in the latter case. The first single state is of pure multireference character showing the equal mixture of [20] + [02] configurations, where the pairs of electrons are distributed over the top-energy e'' level.

The DFT broken symmetry B3LYP/def2-TZVPP level (for all atoms) calculations of $\mathbf{2}^{\mathrm{HOPT}}$ resulted in the $E_{\mathrm{HS}} - E_{\mathrm{BS}}$ gap of -28.51 cm^{-1}, which corresponds to $J = 56.86$ cm^{-1} (for $\hat{H} = -J\hat{S}_1\hat{S}_2$ formalism) after spin decontamination through the Yamaguchi[58] approach. Since the crystal structure of **2** shows possible weak contacts between the copper atoms and π-systems of the neighboring molecule of the heterometallic complex, the new fragment was constructed by selecting the molecule of **2** and closely located *o*-vanillin ligand to give the $\mathbf{2}^{\mathrm{HOPT}}$·*o*-VanH fragment (Fig. S13†). All H-atoms are optimized, while keeping the positions of the other atoms constrained. The presence of the *o*-vanillin molecule slightly affected the calculated exchange coupling constant, which becomes 55.30 cm^{-1}. These values confirm the ferromagnetic coupling that was determined experimentally (Fig. 2, right). The overestimation of the exchange coupling magnitude can be the result of numerous factors, such as the influence of the nearest environment on the molecule in the solid state. Furthermore, according to the CASSCF studies, the singlet state of **2** possesses multireference character, while the DFT calculations consider both states as the single-reference ones. In this way, it shows the incorrect fundamental description of the electronic structure of **2** by the DFT method, and as a result, the significant overestimation of the exchange coupling predicted by the broken symmetry calculations.

The BS methodology itself has significant limitations arising from the physically unrealistic broken symmetry state, which represents a rather crude approximation to the closed-shell singlet one.[52,59] Another source of error is the estimation of absolute electronic energies through the DFT methods, which has significant dependence on the functional, leading to the development of a huge variety of DFT functionals that can be more or less accurate in specific cases.[60] To illustrate the variability of the results in our case, we screened several general purpose DFT functionals towards the estimation of the exchange couplings in the Cu_2 system in $\mathbf{2}^{HOPT}$, as well as in the reference compound $[Cu_2(H^tBuDea)_2(OAc)_2]$ (H^tBuDea = singly deprotonated *tert*-*N*-butyldiethanolamine), for which the singlet–triplet gap was determined with high precision (J_{exp} = −130.1 cm^{-1}) and confirmed by the high-field EPR investigations.[61] For complex $\mathbf{2}^{HOPT}$, the hybrid functionals B3LYP, M06,[62] TPSSh,[63] and PBE0 gave the spread of the predicted *J* values ranging from 48.78 cm^{-1} to 77.06 cm^{-1} when using the def2-TZVPP basis set for copper atoms, and def2-SVP set for all of the other ones (Table S7†). The meta-GGA TPSS,[64] r^2SCAN[65] and M06L[62] functionals resulted in *J* values from 80.24 to 114.92 cm^{-1}, while the GGA functional BLYP afforded a *J* value of 75.94 cm^{-1}. The range-separated hybrid ωB97M-V and ωB97X-D4 functionals[66,67] gave *J* of 39.9 and 44.18 cm^{-1}. Dependence on the basis was found to be almost negligible, considering the overall spread of exchange couplings. For example, for B3LYP, the use of the def2-QZVPPD/def2-QZVP basis set combination changed the theoretically predicted exchange coupling only to −4.21 cm^{-1} (Table S7†). The B3LYP functional supplied with def2-TZVPP/def2-SVP basis sets predicted the *J* value in the complex $[Cu_2(H^tBuDea)_2(OAc)_2]$ to be −174.88 cm^{-1} (deviation from the experimental value is −44.78 cm^{-1}). Remarkably, the use of larger basis sets (def2-QZVPPD/def2-QZVP)[68] gave a considerably higher deviation of −83.12 cm^{-1} (Table S7†). These results are in line with earlier observations on the variability of the exchange couplings predicted through the DFT broken symmetry methodology.[69] Careful tuning of the theoretical level is necessary for each type of coupled system. For example, the TPSSh functional is known to outperform B3LYP for the case of manganese dimers,[70] while B3LYP performs better for copper and iron compounds.[32,71] For the DFT broken symmetry method, the typical magnitude of deviation from the experimentally determined coupling for binuclear compounds constitutes 50 cm^{-1}. For larger clusters, the BS approach may exhibit even larger errors,[72] which cannot be treated by increasing the basis set level or changing the DFT functional.

Careful estimation of the small gaps between the magnetic states can be done through the difference dedicated configuration interaction (DDCI) methodologies, which consider multiple excitations within all configurations, not only the active space. However, such calculations are computationally extraordinarily heavy when triplet excitations (DDCI3) and sufficiently tight configuration inclusion thresholds (T_{sel} of 1 × 10^{-8} or smaller) are requested.[69] The DDCI2 approach with lighter T_{sel} threshold is known to produce inadequate couplings for Cu2 systems, showing errors that are much higher than that of the DFT broken symmetry.[69] In the present case, we applied the lighter SORCI method for estimating the singlet–triplet gap of the abovementioned reference complex (J_{exp} = −130.1 cm^{-1})[61] using the minimum CAS(2,2) active space, def2-TZVPP basis set for copper atoms and def2-SVP for the other ones. With $T_{sel} = 1 \times 10^{-8}$, the DDCI2 and DDCI3 steps resulted in *J* = 354 and 6 cm^{-1}, respectively, showing a very large deviation from the experimental value. Tightening of the threshold to $T_{sel} = 1 \times 10^{-7}$ gave results of the same magnitude with *J* = 50 and 15 cm^{-1}, respectively. Further increase of the precision would require application of the full MR-DDCI3 with a larger active space, which is not feasible for the system comprising *ca.* 70 atoms under our conditions. Notably, even at this rather crude level, the SORCI calculation time was almost two orders of magnitude longer than that for the DFT broken symmetry ones. Therefore, from the methods tested, the DFT broken symmetry remains the one with the best benefit-to-cost ratio after careful selection of the functional.

Catalytic properties

Complex **1** was tested as a catalyst towards the oxidation of hydrocarbons with hydrogen peroxide under mild conditions. Cyclohexane is among the commonly used model substrates for such studies due to its high C–H bond dissociation energy (BDE, 99.5 kcal mol^{-1})[73] and strong industrial relevance.[74] It is known that catalytic oxidations of liquid alkanes with peroxides are often accelerated by acidic or basic promoters. Among them, nitric acid was found to be the most common promoting agent.[8] Therefore, we started from the evaluation of the catalytic activity of 0.5 mol% (1 × 10^{-3} M) of **1** in the oxidation of cyclohexane (0.2 M) with H_2O_2 (1 M) in the presence of 5 mol% of HNO_3 in acetonitrile at 50 °C. The accumulation of oxygenation products, cyclohexanol and cyclohexanone, is depicted in Fig. 5 (top panel). The reaction exhibits an initial reaction rate of $W_0 = 6.6 \times 10^{-6}$ M s^{-1}, decreasing down to 7.8×10^{-7} M s^{-1} after 5 h of reaction time. These values correspond to the turnover frequencies (TOFs) of 24 and 3 h^{-1}, respectively. The total yield at 5 h is 12% with strong selectivity towards the formation of cyclohexanol (97%). It should be noted that such yield can be considered as notable, keeping in mind the theoretical limit of *ca.* 45% due to the overoxidation.[75]

The catalytic system using trifluoroacetic acid (TFA) as a promoter exhibited similar activity with the yield of 10% after 5 h (Fig. 5, bottom panel). The basic promoter, pyridine, achieved not only the yield of 17%, but also the initial reaction rate of $W_0 = 2.1 \times 10^{-5}$ M s^{-1}, which is almost one order higher than for the HNO_3-promoted reaction. Remarkably, the reaction performed without the additives demonstrated the best yield of 21%, supported by the initial reaction rate of 6.4 × 10^{-6} M s^{-1} (Fig. 5, bottom panel). Notably, although the studied catalytic systems show quite different yields, the formal W_0 values are rather close. An analysis of the initial period of the accumulation plots disclosed the presence of a lag period for the reactions in the presence of pyridine and in the absence of a promoter, where the reaction rate smoothly increases until reaching the maxima in *ca.* 10 min. An empirical application of the sigmoidal Hill equation allowed for extraction of the respective reaction rates, being equal to 1.0 × 10^{-4} and 4.8 × 10^{-5} M s^{-1} at 5.6 and 9.3 min, respectively (Fig. S14†). It should be noted that the former rate is close to the highest ones observed for this type of reaction.[15,75] The

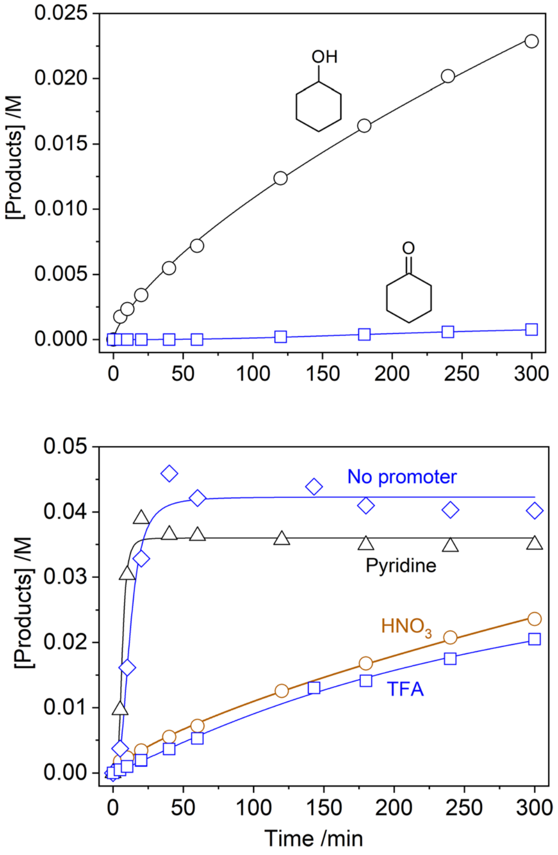

Fig. 5 Accumulations of the reaction products (cyclohexanone and cyclohexanol or their sum) in the oxidation of cyclohexane (0.2 M) with H_2O_2 (1 M) catalyzed by **1** (1 mM) in acetonitrile at 50 °C in the presence of HNO_3 (10 mM) (top), and in the absence or presence of a stated promoter (10 mM) (bottom).

respective lag periods for the acidic-promoted systems are also visible, but much less pronounced.

As catalyst **1** exhibited excellent activity in the absence of promoting additives, we performed further investigations without the use of any promoting agents. First, we tested whether the lag period depends on the catalyst concentration (Fig. S15†). The accumulation curve obtained at 0.11 mol% (2.2×10^{-4} M) catalyst loading is depicted in Fig. 6. As can be seen, the curve has a complex character, which cannot be described as a simple sigmoidal one. The first phase of the reaction shows quasi-linear dependence (0–20 min; $W_0 = 8.3 \times 10^{-7}$ M s^{-1}; TOF = 14 h^{-1}), then demonstrates an acute growth of the reaction rate (20–60 min; $W_{60} = 3.9 \times 10^{-5}$ M s^{-1}; TOF = 636 h^{-1}). Finally, it turns into a completely linear accumulation curve after 60 min ($W_{>60} = 3.9 \times 10^{-6}$ M s^{-1}; TOF = 50 h^{-1}), reaching a maximum at 2 h (total yield 23% and TON = 208). The lag period strongly depends on $[\mathbf{1}]_0$, showing a quasi-linear period of up to 40 min for 0.06 mol% loading ($[\mathbf{1}]_0 = 1.2 \times 10^{-4}$ M), while the highest loading of 0.5 mol% ($[\mathbf{1}]_0 = 1 \times 10^{-3}$ M) results in a nearly visible lag period of less than 5 min. The "breakpoints" with an acute change of the accumulation behavior were observed in all experiments with $[\mathbf{1}]_0 < 7 \times 10^{-4}$ M (Fig. S15†). The test using copper(II) chloride as the catalyst (2.2×10^{-4} M) revealed a regular linear dependence in the 0–80 min range with $W_0 = 3.2 \times 10^{-6}$ M s^{-1} (Fig. S15†). Therefore, the lag periods (Fig. 6) were associated with catalyst **1**. The test using 0.35 mol% (7×10^{-4} M) of complex **2** as a catalyst also disclosed the lag period, with the product yield of 18% after 3 h (Fig. S15†).

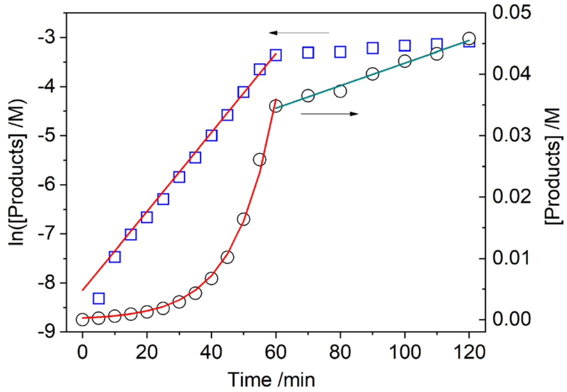

Fig. 6 Accumulation of the reaction products (circles; sum of cyclohexanone and cyclohexanol) in the oxidation of cyclohexane (0.2 M) with H_2O_2 (1 M) catalyzed by **1** (2.2×10^{-4} M) in acetonitrile at 50 °C. Square symbols show the logarithm of the concentration. Solid red lines represent the exponential fit of the 0–60 min range, and the dark green line shows a linear fit of the 60–120 min period.

The strong influence of a catalyst concentration on the quasi-linear period suggests the transformation of a catalyst with the appearance of new, highly active species. Therefore, the complex accumulation curves for **1** can be explained by assuming the following model. As the reaction is expected to be a non-chain free radical one, one mole of the oxidant, H_2O_2, is catalytically transformed into one mole of the hydroxyl radicals, $HO^{\bullet}$.[76] Participation of the hydroxyl radicals as the species that abstract H-atoms from the hydrocarbon substrate is expected for catalytic systems based on the copper catalyst and the hydrogen peroxide oxidant. In this reaction, the interaction of H_2O_2 with the Cu(II) centre results in the reduction of a copper catalyst with the release of a weakly active $HOO^{\bullet}$ radical (4).[8,75,76] Reaction of a second H_2O_2 molecule with the reduced catalyst state affords the $HO^{\bullet}$ radical and oxidized Cu(II) state, closing the catalytic cycle (5).

$$Cu^{II} + H_2O_2 \rightarrow Cu^{I} + HOO^{\bullet} + H^{+} \quad (4)$$

$$Cu^{I} + H_2O_2 \rightarrow Cu^{II} + HO^{-} + HO^{\bullet} \quad (5)$$

$$RH + HO^{-} \rightarrow R^{\bullet} + H_2O \quad (6)$$

$$R^{\bullet} + O_2 \rightarrow ROO^{\bullet} \quad (7)$$

$$ROO^{\bullet} + Cu^{I} + H^{+} \rightarrow Cu^{II} + ROOH \quad (8)$$

Abstraction of the H atom from the substrate results in a series of transformations, from which the principal ones are shown *via* eqn (6)–(8). The final product is alkyl hydroperoxide, which can be observed directly (through the GCMS technique),[77] or indirectly by measuring the alcohol/ketone ratio before and after treatment of the sample with a reducing agent (*e.g.*, PPh_3).[78] The low bond and stereoselectivities (see ESI, Scheme S1†) exhibited by the $\mathbf{1}/H_2O_2$ and $\mathbf{2}/H_2O_2$ catalytic systems unambiguously indicate[79] the attack of C–H bonds by the $HO^{\bullet}$ radical generated through the Fenton-like reactions (4) and (5).

The observed rate of product (cyclohexanol and cyclohexanone) formation W_P can be treated as the rate of catalytic generation of hydroxyl radicals $W_{HO^{\bullet}}$, corrected with a linear coefficient k_{corr}, $W_P = k_{corr}W_{HO^{\bullet}}$, which includes factors such as the reaction of the hydroxyl radicals with an acetonitrile solvent. The presence of a lag period with the subsequent exponential growth is typical for autocatalytic reactions.[80] The "breakpoints" at the end of the exponential step suggest that the autocatalytic process involves rapid transformation of the catalyst, which depletes at the "breakpoint". The further linear accumulation could be associated with the activity of the copper species originating from the degraded catalyst, as the respective reaction rates are close to those exhibited by copper(II) chloride (Fig. S15†).

The overall process starts with complex **1** slowly reacting with H_2O_2 (k_1). This first phase corresponds to the quasi-linear period, clearly observed for low catalyst loadings (Fig. 6 and S15†). Under the experimental conditions, catalyst **1** undergoes a gradual transformation (k_2) into the species **1*** having much higher catalytic activity in $HO^{\bullet}$ radical generation ($k_3 \gg k_1$) and having a short lifetime (k_4). The fast generation of hydroxyl radicals by **1*** results in accelerated **1** → **1*** transformation in this way, closing the autocatalytic cycle. When all of the starting catalyst **1** is depleted, the reaction reaches a breakpoint, showing only the residual activity of the degradation products [Cu] (k5).

$$\mathbf{1} + H_2O_2 \rightarrow HO^{\bullet} \qquad (k1)$$

$$\mathbf{1} + HO^{\bullet} \rightarrow \mathbf{1^*} \qquad (k2)$$

$$\mathbf{1^*} + H_2O_2 \rightarrow HO^{\bullet} \qquad (k3)$$

$$\mathbf{1^*} \rightarrow [Cu] \qquad (k4)$$

$$[Cu] + H_2O_2 \rightarrow HO^{\bullet} \qquad (k5)$$

The logarithm of the reaction product concentration shows a nearly linear dependence in the 0–60 min range for $[\mathbf{1}]_0 = 2.2 \times 10^{-4}$ M (Fig. 6). The exponential fit using the first-order equation $C = C_0e^{kt}$ resulted in $k_{eff} = 1.3 \times 10^{-3}$ s^{-1}. The chemical meaning of the constant k_{eff} is limited because it accumulates all the reaction constants k_1–k_5. However, keeping in mind the conditions $k_3 \gg k_1$ and $k_3 \gg k_5$, one can conclude that $k_{eff} \sim k_3$. The use of a large excess (0.4 M) of the substrate bearing a weak tertiary C–H bond (methylcyclohexane) had a slight influence on the products accumulation and a "breakpoint" position (Fig. S14†), suggesting that consumption of hydroxyl radicals by the substrate has a limited effect on the **1*** formation rate. Complexes **1** and **2** were tested towards the oxidation of various hydrocarbons (see the ESI†). The observed normalized bond selectivities agree with the participation of hydroxyl radicals as the H-abstracting species.

UV/Vis spectroscopy

The UV/Vis spectra of complex **1** (3.1×10^{-4} M) in acetonitrile solution of water (3.1 M) and nitromethane (0.34 M) as a function of time are depicted in Fig. 7. These conditions reproduce those used for promoter-free catalytic studies, except for the presence of H_2O_2. The starting spectrum in the 300–800 nm range features a strong peak at 362 nm and two broad weak absorptions at 430 nm and 470 nm. The visible part of the spectrum shows gradual alteration with time, where the latter peaks exhibit an increase of absorption intensity, while the peak at 362 nm has negligible changes within 2 nm. Since the absorption at 362 nm undergoes a huge shift upon decoordination of the ligand (326 nm and 344 for free HL and *o*-vanil-

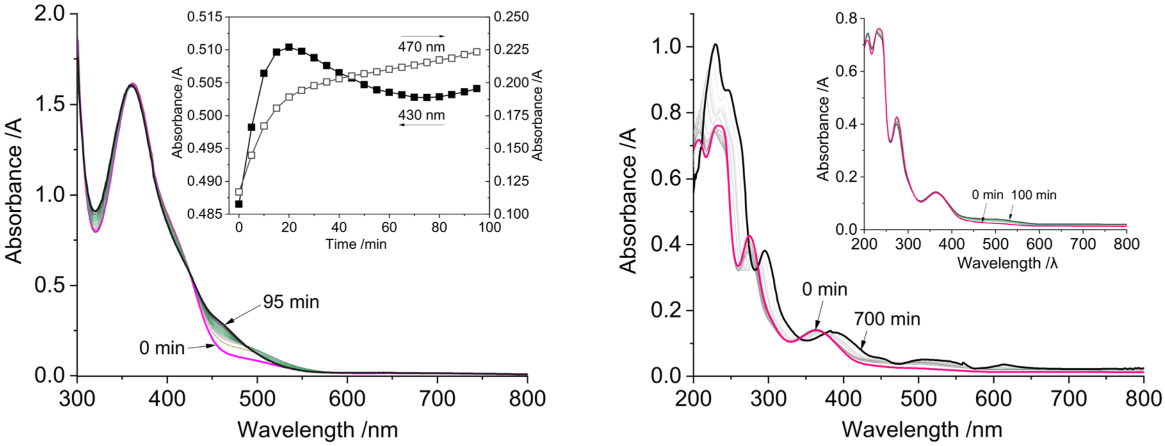

Fig. 7 Left: UV/Vis spectra of the complex **1** (3.1×10^{-4} M) in acetonitrile containing H_2O (3.1 M) and nitromethane (0.34 M) recorded every 5 min at room temperature. The inset shows the intensities of 430 and 470 nm absorptions as a function of time. Right: UV/Vis spectra of **2** (7.3×10^{-6} M) in acetonitrile recorded every 10 min at room temperature. The inset shows the spectra recorded for up to 100 min time.

lin in acetonitrile, respectively, Fig. S16†), the above slight alterations of the 430 and 470 nm bands can be rather associated with the gradual solvation of a molecule of **1** which dinuclear structure is preserved. The spectrum of complex **2** in acetonitrile in the 300–800 nm range features a strong peak at 365 nm wavelength and a very broad absorption centred approximately at 500 nm (Fig. 7). The UV region of **2** shows strong peaks at 207, 234 and 275 nm. In contrast to **1**, the spectrum of **2** does not demonstrate notable alterations within 100 min time, just showing a gradual increase of 500 nm absorption intensity (Fig. 7, right, inset). However, after *ca.* 400 min the spectrum of **2** starts to change substantially, leading to distorted lines at 700 min, indicative of the formation of a precipitate due to the degradation of the coordination compound.

UV/Vis spectra measured for complex **1** in the presence of a slight excess (1.8 eq.) of H_2O_2 are depicted in Fig. 8, left. After addition of H_2O_2 the new broad absorption band at 460 nm appears. The spectrum undergoes evolution with time, where the largest changes are observed at 410 and 490 nm absorptions, first showing significant increase of the intensity with the subsequent decay to initial levels (Fig. 8, left, inset). At the same time, the absorption at *ca.* 360 nm shows only slight variations in intensity and wavelengths (Fig. 8, left), indicating that the aromatic ligands remain coordinated to the metal centres. The spectral changes observed upon reaction of **1** with H_2O_2 can be understood in terms of coordination of a hydrogen peroxide molecule to a molecule of **1** with subsequent reduction of the copper centre. An attempt to reproduce this process was performed by recording the spectra after mixing equimolar amounts of **1** and PPh_3 in acetonitrile (Fig. 8, right). As can be seen, the spectra exhibit gradual growth of the broad band at 490 nm. The kinetics of the absorbance at 490 nm resembles the 1st order reaction. Reduction of Cu(II) to Cu(I) by PPh_3 with formation of $PPh_3{=}O$ in the presence of air is a known process for compounds of copper.[81] The catalytic test with pre-reduction of the catalyst **1** by 1.5 equivalents of PPh_3 before addition of H_2O_2 afforded expected color changes of the solution from green (pure **1**) to brown (**1** + PPh_3). However, the lag period and the catalytic parameters were not affected by this procedure. Therefore, the observed lag period (Fig. 6) cannot be associated to the initial formation of presumable Cu(I) intermediates. Also, the position of the 362 nm peak observed for **1** (Fig. 7, left) remains almost unchanged for the **1** + PPh_3 mixture (360 nm, Fig. 8, right), indicating the absence of long-lived Cu(I) species for which an immense shift of the absorption band is expected (see below).

DFT/TDDFT assessment of behaviour of 1 in solution

The electronic structures of complex **1** and the presumable intermediates in acetonitrile were studied to confirm the assignment of the spectral changes to the Cu(II)/Cu(I) redox reactions. The square-planar coordination environment of the copper centre in the molecule of **1** (Fig. 1, top) presumes the $^2B_{1g}$ ground state with the unpaired electron located in the $d_{x^2-y^2}$ orbital.

DFT optimization of the geometry of **1** starting from the X-ray coordinates was performed at the PBE0/ma-def2-SVP(ma-def2-TZVP for Cu and Cd) level (structure $\mathbf{1}^{\mathrm{OPT}}$). The optimized structure maintains a planar structure of the molecule, as expected for the Cu(II) coordination geometry. As the pure planar environment is not likely to persist in the coordinating solvent, the respective model $\mathbf{1}^{\mathrm{OPT}}{\cdot}2CH_3CN$ was considered where two acetonitrile molecules saturate the apical positions of the copper centre. The TDDFT spectra of $\mathbf{1}^{\mathrm{OPT}}$ and

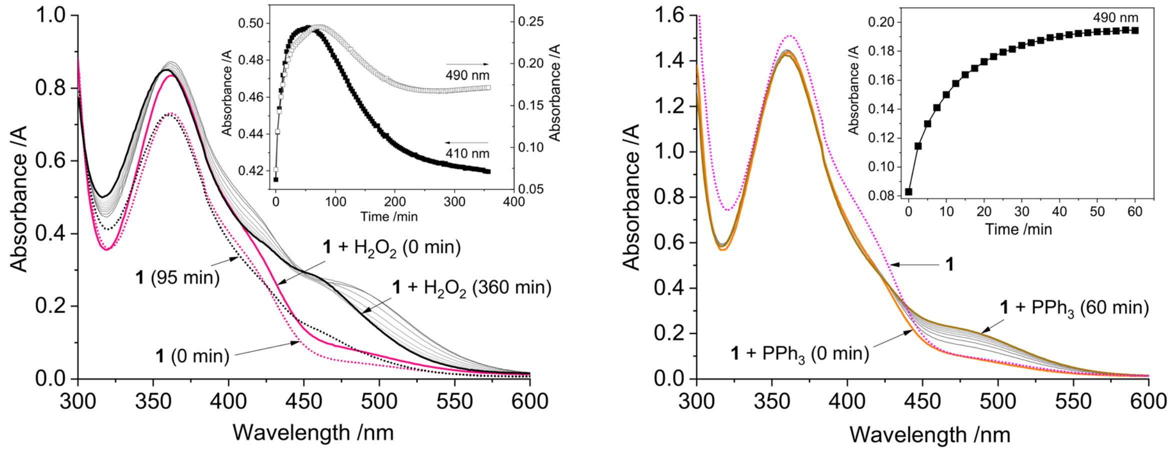

Fig. 8 Left: Dotted lines: UV/Vis spectra of the complex **1** (1.4×10^{-4} M) after dissolution (purple dotted line) and after 95 min (black dotted line). Solid lines: Evolution of the spectra of **1** (1.4×10^{-4} M) with time in the presence of H_2O_2 (2.5×10^{-4} M) in acetonitrile at room temperature. The inset shows the absorptions at 410 and 490 nm. Right: Dotted line: UV/Vis spectrum of complex **1** (2.9×10^{-4} M) after dissolution (purple dotted line). Solid lines: Evolution of the spectra of **1** (2.9×10^{-4} M) with time after the addition of an equimolar amount of PPh_3 in acetonitrile at room temperature. The inset shows the absorption at 490 nm.

$\mathbf{1}^{\mathrm{OPT}}\cdot 2CH_3CN$ calculated at the DKH-PBE0/aug-cc-pVDZ(aug-cc-pVTZ for Cu and Cd)[82–86] level of theory are depicted in Fig. 9. The PBE0 hybrid functional has a reasonable accuracy for estimating the excited states,[32,87] while the aug-cc-pVxZ basis set family is generally recommended for TDDFT studies.[88] The calculated spectra of $\mathbf{1}^{\mathrm{OPT}}$ and $\mathbf{1}^{\mathrm{OPT}}\cdot 2CH_3CN$ are similar in the UV range. In contrast, the weak absorptions in the visible region (Fig. 9, left, inset) demonstrate significant differences, where the compound with coordinated acetonitrile molecules reveals an absorption band (after Gauss broadening) at 600 nm originated from the copper d–d transitions. The predicted characteristic absorption at 345 nm is close to that observed experimentally (362 nm, Fig. 7). This absorption band consists of the two strong vertical transitions at 336 and 357 nm (Fig. 9, right). The natural transition orbital analysis confirms that both these excited states consist mainly of two groups of transitions, each between highly delocalized π-orbitals of the aromatic ligands (Fig. S17†). Thus, they are irrelevant to the presence of coordinated acetonitrile molecules. Therefore, the experimental absorption band at 362 nm depends only on the mutual configuration of the organic ligands and can serve as an indicator if the ligands are coordinated to metal centres in solution. The TDDFT calculations of a similar configuration $\mathbf{1}^{\mathrm{OPT}}\cdot 2CH_3CN$ with water molecules instead of acetonitrile ones also demonstrated the irrelevance of the above absorption band to the coordinated solvent molecules (Fig. 9). The TDDFT calculations for the free ligand HL and *o*-vanillin in acetonitrile medium (Fig. S18†), show the energies of the first excited state of 338 and 311 nm for *o*-vanillin and HL, respectively (the experimental values for *o*-vanillin and HL are 344 and 326 nm, respectively).

The search for the geometry of the putative species containing the Cu(I) centre has started from the DFT optimization of the structure of $\mathbf{1}^{\mathrm{OPT}}\cdot 2CH_3CN$ with the singlet ground state and −1 charge. The expected distortion of the coordination geometry of Cu(I) results in two possible conformations, $\mathbf{1}^{\mathrm{Ia}}\cdot 2CH_3CN$ and $\mathbf{1}^{\mathrm{Ib}}\cdot 2CH_3CN$ (Fig. S19†), with the energies differing by 0.69 kcal mol^{-1} in favor to $\mathbf{1}^{\mathrm{Ib}}\cdot 2CH_3CN$. The TDDFT calculations suggested that both structures would have a broad absorption in the 500–600 nm region and a new band at 380 nm (Fig. S22†). Due to the low difference in energy, both presumable structures can exist in solution simultaneously; thus, an averaged spectrum was constructed. The characteristic peaks expected for π → π* transitions within the ligands exhibit a shift down to 326 nm. Such an increase of the energy compared to that predicted for Cu(II) structures (345 nm) can be explained by the involvement of copper d-orbitals into the ground state orbital resulting in lowering of its energy. However, it can be seen that the reaction of **1** with PPh_3 does not afford the shift of the 362 nm absorption peak. Moreover, the respective experimental spectra do not exhibit a notable absorption at 600 nm (Fig. 8, right). The next considered model was the elimination of a chloride anion from $\mathbf{1}^{\mathrm{I}}\cdot 2CH_3CN$ compounds with subsequent coordination of a third acetonitrile molecule to a cadmium centre. The optimized structures of $\mathbf{1}^{\mathrm{Ia}}\cdot 3CH_3CN$ and $\mathbf{1}^{\mathrm{Ib}}\cdot 3CH_3CN$ are depicted in Fig. S20,† where the compound $\mathbf{1}^{\mathrm{Ia}}\cdot 3CH_3CN$ is 3.23 kcal mol^{-1} more stable than $\mathbf{1}^{\mathrm{Ib}}\cdot 3CH_3CN$. The TDDFT calculated spectra of these compounds are different in the visible region, where the compound $\mathbf{1}^{\mathrm{Ia}}\cdot 3CH_3CN$ exhibits an absorption band at 440 nm, while the compound $\mathbf{1}^{\mathrm{Ia}}\cdot 3CH_3CN$ shows a strong absorption band at 546 nm. The 440 nm band in the calculated broadened spectrum of $\mathbf{1}^{\mathrm{Ia}}\cdot 3CH_3CN$ is stipulated by the excited state at 22 088 cm^{-1} (458 nm) constructed of a single MLCT transition (96%) from the HOMO orbital, containing 63.4% of copper d-orbitals to the LUMO one, mostly localized on aromatic ring of the *o*-vanillin ligand (Fig. S22,† right).

Although the TDDFT-predicted spectrum of $\mathbf{1}^{\mathrm{Ia}}\cdot 3CH_3CN$ contains the absorption band in the region of 440 nm (Fig. S22†), which is close to the experimentally observed at 490 nm (Fig. 8, right), the common feature of all calculated Cu(I)-derivatives of **1** is the significant shift of the characteristic π → π* absorption from 345 to 326 nm (predicted values) due to distortion of the planar mutual disposition of aromatic

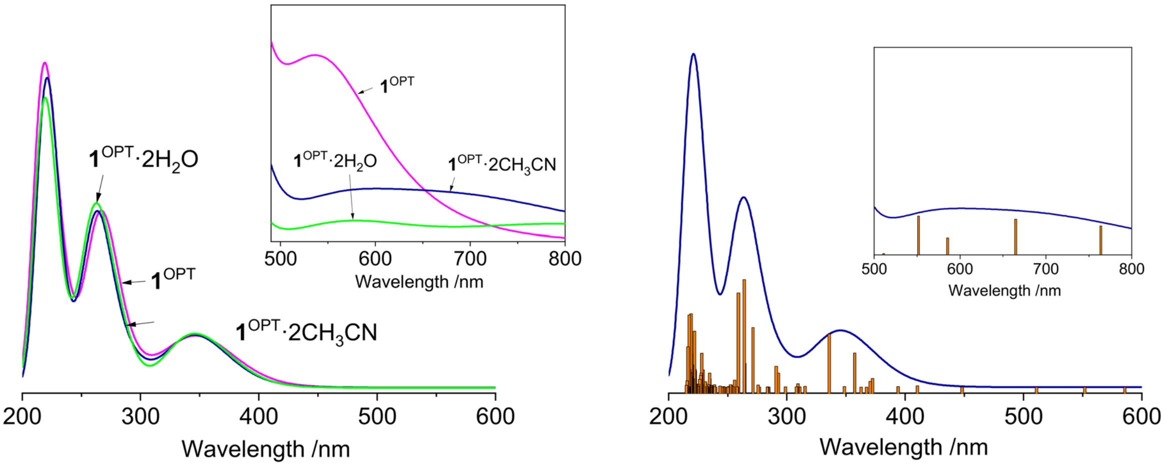

Fig. 9 Left: TDDFT spectra of $\mathbf{1}^{\mathrm{OPT}}$, $\mathbf{1}^{\mathrm{OPT}}\cdot 2CH_3CN$ and $\mathbf{1}^{\mathrm{OPT}}\cdot 2H_2O$ calculated at the DKH-PBE0/aug-cc-pVDZ(aug-cc-pVTZ for Cu and Cd) level in acetonitrile (SMD solvation model). Right: TDDFT calculated spectrum for $\mathbf{1}^{\mathrm{OPT}}\cdot 2CH_3CN$ showing the vertical transition energies.

ligands. In contrast, in all of the experimental spectra, the wavelength of the respective peak (*ca.* 360 nm) remains practically unchanged (Fig. 7 and 8). This indicates that the long-lived Cu(I) species are not likely to be explanation for absorptions appearing in the visible region upon reaction of **1** with H_2O_2 or PPh_3. Thus, the model containing the PPh_3 ligand coordinated to the Cu(II) centre in **1** was constructed and DFT optimized ($\mathbf{1}^{OPT}\cdot CH_3CN\cdot PPh_3$, Fig. S21†). The coordination geometry around the copper centre is a square-pyramidal one with the apical Cu–P distance of 2.784 Å. Such a rather large distance as compared to that expected for Cu^{II}–PPh_3 one (2.3–2.4 Å)[89,90] can be explained by steric repulsion of the PPh_3 phenyl ligands and those from the heterometallic molecule. The TDDFT calculated spectrum of $\mathbf{1}^{OPT}\cdot CH_3CN\cdot PPh_3$ is depicted in Fig. S23.† As can be seen, the position of the characteristic peak in the UV region remains practically unaltered (340 nm). The spectrum exhibits an elevated absorption in the 400–500 nm region due to the presence of vertical transitions at 399 and 417 nm. The latter is composed mostly of the ligand to metal charge transfer (LMCT) π → d band. Although the position and absorption strength of this band are not sufficient for direct interpretation of the strong absorbance in the visible region upon addition of PPh_3 to **1** (Fig. 8, right), one may conclude that these absorptions have similar nature.

The possibility of the formation of oxidized forms of **1** was probed by modelling the cationic structure $\mathbf{1}^{ox}\cdot 2CH_3CN$ having 1+ charge and triplet spin state. DFT optimization of $\mathbf{1}^{ox}\cdot 2CH_3CN$ resulted in a slight distortion of the planar geometry of the ligands. Analysis of the spin density revealed that one unpaired electron remains on the copper $d_{x^2-y^2}$ orbital, while the other one is localized on the π-type molecular orbital of the Schiff-base ligand involving coordinated N,O-atoms (Fig. S24†). Meanwhile, the *o*-Van⁻ ligand remains intact. The broken symmetry calculations at the B3LYP/def2-TZVPP level confirmed the triplet ground spin state of $\mathbf{1}^{ox}\cdot 2CH_3CN$ with the formal coupling constant $J = 174.8\ cm^{-1}$. The TDDFT calculations suggest that the UV/Vis spectrum of $\mathbf{1}^{ox}\cdot 2CH_3CN$ should not differ much from that for $\mathbf{1}^{OPT}\cdot 2CH_3CN$ with the only difference in the visible region where a strong band at 746 nm appears (Fig. S24†). Analysis of the natural transition orbitals associated with the respective excited state S_3 disclosed the π → π nature of this transition. The experimental UV/Vis spectra of the $\mathbf{1}/H_2O_2$ mixture do not exhibit an absorbance at such a low energy (Fig. 8). Thus, even considering the deviation between TDDFT-predicted and true energies of excited states, the existence of long-lived ligand-oxidized species can be ruled out in the present catalytic reaction.

DFT calculations of electron affinity of 1

The cyclic voltammetry of **1** indicated that the single-electron reduction of copper Cu(II) → Cu(I) is an unfavorable process (Fig. S4†). The same conclusion was indirectly suggested by the UV and TDDFT studies, where the absence of a shift of 362 nm absorption indicated the stability of the planar Cu(II) configuration of the complex under the catalytic conditions, as well as upon reaction with the reductant (PPh_3). Considering the importance of the Cu(II) ⇌ Cu(I) interconversions for the catalytic cycle, the high energy barrier of this reduction process may explain the low initial reaction rates in the oxidations with H_2O_2 (Fig. 6).

Table 1 DFT calculated vertical and adiabatic electron affinities for selected complexes[a]

	Vertical		Adiabatic		
	kcal mol⁻¹	eV	kcal mol⁻¹	eV	Ref.
$\mathbf{1}^{OPT}$	66.10	2.87	81.46	3.53	t. w.[b]
$\mathbf{1}^{OPT}\cdot 2CH_3CN$	56.77	2.46	77.86	3.38	t. w.
$\mathbf{1}^{Ia}\cdot 3CH_3CN$	62.58	2.71	83.49	3.62	t. w.
$[Cu(L^1)_2(H_2O)_2]^{2+}$ [c]	82.47	3.58	106.62	4.62	33
$[Cu(L^1)(OAc)_2]$	56.51	2.45	81.93	3.55	33
$[Cu(L^2)(CH_3CN)]^{2+}$ [d]	82.77	3.59	93.96	4.07	92

[a] Structures optimized at the PBE0/ma-def2-SVP(ma-def2-TZVP for Cu and Cd) level in acetonitrile C-PCM implicit solvation model. [b] This work. [c] Starting coordinates from the CSD refcode RELBOC. [d] Starting coordinates from the CSD refcode HEQWEF; L^1 = bis(3,5-dimethylpyrazol-1-yl)methane; L^2 = tris(2-pyridylmethyl)amine.

The probability of a reduction process can be described as the relative level of electron affinity of the compound. The latter can be calculated from the ground state energies of the neutral and reduced species: $EA = E^0 - E^-$ using unrelaxed (vertical electron affinity) or relaxed (adiabatic electron affinity) geometry.[91] The electron affinities calculated for the DFT optimized species of **1** and some representative literature examples are listed in Table 1. As can be seen, both vertical and adiabatic electron affinities for the compounds clearly reflect the appearance of the Cu(II) ⇌ Cu(I) waves in the cyclic voltammograms. $[Cu(L^1)_2(H_2O)_2](ClO_4)_2$ and $[Cu(L^2)(CH_3CN)](OTf)_2$,[33,92] are approximately 1 eV higher than those which do not show such an ox-red process (**1** and $[Cu(L^1)(OAc)_2]$). This effect cannot be associated with the cationic nature of the first two complexes because the model $\mathbf{1}^{Ia}\cdot 3CH_3CN$ is also a cationic one (it has 1+ charge due to replacement of Cl⁻ with CH_3CN). Therefore, the Cu(II) → Cu(I) reduction process is disfavored in complex **1**, resulting in the suppression of its catalytic activity at the initial phase of the catalytic reaction.

Conclusions

In summary, we have reported the synthesis and crystal structures of two novel heterometallic coordination compounds $[Cu^{II}Cd^{II}ClL(o\text{-}Van)(OAc)]\cdot 3H_2O$ (**1**) and $[Cu^{II}_2Zn^{II}Cl_2L_2(o\text{-}Van)(OAc)]$ (**2**), resulting from the interaction of a fine copper powder and Cd(II) or Zn(II) acetate with methanol solution of the Schiff-base ligand HL formed *in situ*. The structures of both compounds were determined by the single-crystal X-ray diffraction, presenting heterometallic molecular cores, where metal atoms are joined by oxygen bridges of deprotonated *o*-vanillin, Schiff base L^- (for **1** and **2**) and acetate (for **2**) ligands. The magnetic investigations revealed a pronounced out-of-phase signal for the $Cu^{II}Cd^{II}$ complex **1** indicating the presence of slow magnetic relaxation under applied magnetic field. The observable relaxation of the isolated paramagnetic Cu(II) compounds is a rare effect which herein was associated with appreciable anisotropy of the *g*-factor, confirmed by the EPR spectroscopy and CASSCF theoretical calculations. Complex **2** is a weakly coupled ferromagnet. Both ground state triplet and broken symmetry states for **2** have strong multireference character, as found from the CASSCF/NEVPT2 studies. Complexes **1** and **2** act as catalysts for the homogeneous oxidation of hydrocarbons with H_2O_2 under mild conditions. **1** shows the catalytic behaviour of remarkable complexity with several distinct kinetic phases, indicating transformations of the coordination compound under the catalytic conditions. Together with the TD-DFT calculations, the UV/Vis spectroscopy results disclosed possible configurations of complex **1** in solution, where it maintains its planar structure during the catalytic oxidation of substrates. The cyclic voltammetry and theoretical electron affinity investigations evidenced that the Cu(II) → Cu(I) reduction process is highly unfavorable for **1**, thus explaining the suppression of the catalytic activity of the compound at the initial phases of the reaction.

Finally, the work has extended the synthetic approach towards the preparation of heterometallic heteroleptic compounds of transition metals starting from metal powders, and provided new data on the slow magnetic relaxation in the $S = 1/2$ systems. It has demonstrated that the second redox-inactive metal has a strong influence on the catalytic behavior of the catalytically active centre through the supporting specific coordination geometry around the active metal centre.

Author contributions

O. Yu. V.: conceptualization, funding acquisition, writing – original draft and editing; O. V. N.: conceptualization, methodology, catalytic studies, theoretical calculations, writing – original draft and editing; A. B.: magnetic and EPR data analysis, writing – original draft and editing; U. K. K.: magnetic data collection and treatment; E. A. B.: synthesis and characterization of compounds; S. M. V.: electrochemical studies, writing – original draft; B. W. S.: X-ray crystallographic studies; D. S. N.: conceptualization, theoretical calculations, visualization, project administration, writing – original draft and editing. The manuscript was written through contributions of all authors. All authors have given approval to the final version of the manuscript.

Data availability

The crystallographic CIF files have been submitted to the Cambridge Crystallographic Data Centre and have received the following CCDC numbers: CCDC 1958659 (**1**) and 1960155 (**2**).

The ESI† file provided with this submission contains data in several formats. The Schemes and Figures describe the supplementary catalytic reaction details, molecular structures, isosurfaces of the natural transition orbitals, and UV-Vis and EPR spectra of the compounds, including the modelled ones. The Tables contain the supplementary crystallographic data. The Listings show the sample ORCA inputs used in this work and the selected output for CASSCF calculations.

The atomic coordinates of the molecular structures obtained from the DFT quantum chemical simulations are provided as part of the ESI.†

Conflicts of interest

There are no conflicts to declare.

Acknowledgements

This work was funded by the Ministry of Education and Science of Ukraine (grant for the perspective development of the scientific direction “Mathematical sciences and natural sciences” at the Taras Shevchenko National University of Kyiv). The authors acknowledge the OBLIVION Supercomputer (HPC Centre of the University of Évora, Portugal) funded by the “Enabling Green E-science for the SKA Research Infrastructure (ENGAGE SKA)”, reference POCI-01-0145-FEDER-022217 (COMPETE 2020), and Foundation for Science and Technology (FCT), Portugal. This work was supported by computational resources from FCT I.P. under projects 2024.02988.CPCA.A0 (O.V.N.) and 2023.10683.CPCA.A1 (D.S.N.).

References

1 X. Y. Huang and J. T. Groves, *Chem. Rev.*, 2018, **118**, 2491–2553.

2 V. C. C. Wang, S. Maji, P. R. Y. Chen, H. K. Lee, S. S. F. Yu and S. I. Chan, *Chem. Rev.*, 2017, **117**, 8574–8621.

3 S. Sirajuddin and A. C. Rosenzweig, *Biochemistry*, 2015, **54**, 2283–2294.

4 P. R. O. de Montellano, *Chem. Rev.*, 2010, **110**, 932–948.

5 P. Gandeepan, T. Muller, D. Zell, G. Cera, S. Warratz and L. Ackermann, *Chem. Rev.*, 2019, **119**, 2192–2452.

6 M. C. Gao, R. X. Ye, W. J. Shen and B. Xu, *Org. Biomol. Chem.*, 2018, **16**, 2602–2618.

7 F. Wang, P. H. Chen and G. S. Liu, *Acc. Chem. Res.*, 2018, **51**, 2036–2046.

8 D. S. Nesterov, O. V. Nesterova and A. J. L. Pombeiro, *Coord. Chem. Rev.*, 2018, **355**, 199–222.

9 S. Hong, F. F. Pfaff, E. Kwon, Y. Wang, M.-S. Seo, E. Bill, K. Ray and W. Nam, *Angew. Chem., Int. Ed.*, 2014, **53**, 10403–10407.

10 Y. Morimoto, H. Kotani, J. Park, Y.-M. Lee, W. Nam and S. Fukuzumri, *J. Am. Chem. Soc.*, 2011, **133**, 403–405.

11 E. Y. Tsui, R. Tran, J. Yano and T. Agapie, *Nat. Chem.*, 2013, **5**, 293–299.

12 O. V. Nesterova, K. V. Kasyanova, V. G. Makhankova, V. N. Kokozay, O. Y. Vassilyeva, B. W. Skelton, D. S. Nesterov and A. J. L. Pombeiro, *Appl. Catal., A*, 2018, **560**, 171–184.

13 O. V. Nesterova, K. V. Kasyanova, E. A. Buvaylo, O. Y. Vassilyeva, B. W. Skelton, D. S. Nesterov and A. J. L. Pombeiro, *Catalysts*, 2019, **9**, 15.

14 O. V. Nesterova, M. L. Kuznetsov, A. J. L. Pombeiro, G. B. Shul'pin and D. S. Nesterov, *Catal. Sci. Technol.*, 2022, **12**, 282–299.

15 D. S. Nesterov, E. N. Chygorin, V. N. Kokozay, V. V. Bon, R. Boča, Y. N. Kozlov, L. S. Shul'pina, J. Jezierska, A. Ozarowski, A. J. L. Pombeiro and G. B. Shul'pin, *Inorg. Chem.*, 2012, **51**, 9110–9122.

16 L. K. G. Ackerman-Biegasiewicz, S. K. Kariofillis and D. J. Weix, *J. Am. Chem. Soc.*, 2023, **145**, 6596–6614.

17 P. Buchwalter, J. Rose and P. Braunstein, *Chem. Rev.*, 2015, **115**, 28–126.

18 E. N. Chygorin, V. N. Kokozay, I. V. Omelchenko, O. V. Shishkin, J. Titiš, R. Boča and D. S. Nesterov, *Dalton Trans.*, 2015, **44**, 10918–10922.

19 O. V. Nesterova, D. S. Nesterov, B. Vranovicova, R. Boča and A. J. L. Pombeiro, *Dalton Trans.*, 2018, **47**, 10941–10952.

20 O. Y. Vassilyeva, E. A. Buvaylo, V. N. Kokozay, B. W. Skelton, A. N. Sobolev, A. Bieńko and A. Ozarowski, *Dalton Trans.*, 2021, **50**, 2841–2853.

21 V. N. Kokozay, O. Y. Vassilyeva and V. G. Makhankova, in *Direct Synthesis of Metal Complexes*, ed. B. Kharisov, Elsevier, Amsterdam, 2018.

22 D. S. Nesterov, O. V. Nesterova, V. N. Kokozay and A. J. L. Pombeiro, *Eur. J. Inorg. Chem.*, 2014, 4496–4517.

23 E. N. Chygorin, O. V. Nesterova, J. A. Rusanoya, V. N. Kokozay, V. V. Bon, R. Boča and A. Ozarowski, *Inorg. Chem.*, 2012, **51**, 386–396.

24 V. V. Semenaka, O. V. Nesterova, V. N. Kokozay, R. I. Zybatyuk, O. V. Shishkin, R. Boča, C. J. Gomez-Garcia, J. M. Clemente-Juan and J. Jezierska, *Polyhedron*, 2010, **29**, 1326–1336.

25 D. S. Nesterov, C. Graiff, A. Tiripicchio and A. J. L. Pombeiro, *CrystEngComm*, 2011, **13**, 5348–5353.

26 O. V. Nesterova, A. V. Lipetskaya, S. R. Petrusenko, V. N. Kokozay, B. W. Skelton and J. Jezierska, *Polyhedron*, 2005, **24**, 1425–1434.

27 O. V. Pryma, S. R. Petrusenko, V. N. Kokozay, O. V. Shishkin and M. V. Zhigalko, *Inorg. Chem. Commun.*, 2003, **6**, 896–899.

28 V. N. Kokozay, E. V. Polunkin, O. Y. Vassilyeva, T. M. Kameneva, V. S. Pilyavskiy and B. W. Skelton, *Theor. Exp. Chem.*, 2022, **58**, 213–219.

29 O. Y. Vassilyeva, V. N. Kokozay and B. W. Skelton, *Issues Chem. Chem. Technol.*, 2023, 41–50, DOI: 10.32434/0321-4095-2023-147-2-41-50.

30 C. F. Matta and R. J. Boyd, An Introduction to the Quantum Theory of Atoms in Molecules in *The Quantum Theory of Atoms in Molecules: From Solid State to DNA and Drug Design*, ed. C. F. Matta and R. J. Boyd, Wiley, 2007.

31 G. Saleh, C. Gatti, L. Lo Presti and J. Contreras-Garcia, *Chem. – Eur. J.*, 2012, **18**, 15523–15536.

32 O. V. Nesterova, O. Y. Vassilyeva, B. W. Skelton, A. Bieńko, A. J. L. Pombeiro and D. S. Nesterov, *Dalton Trans.*, 2021, **50**, 14782–14796.

33 A. P. Sandoval-Rojas, L. Ibarra, M. T. Cortés, M. A. Macías, L. Suescun and J. Hurtado, *J. Electroanal. Chem.*, 2017, **805**, 60–67.

34 S. Reinoso, P. Vitoria, J. M. Gutiérrez-Zorrilla, L. Lezama, L. San Felices and J. I. Beitia, *Inorg. Chem.*, 2005, **44**, 9731–9742.

35 N. F. Chilton, R. P. Anderson, L. D. Turner, A. Soncini and K. S. Murray, *J. Comput. Chem.*, 2013, **34**, 1164–1175.

36 A. Prokofieva, A. I. Prikhod'ko, E. A. Enyedy, E. Farkas, W. Maringgele, S. Demeshko, S. Dechert and F. Meyer, *Inorg. Chem.*, 2007, **46**, 4298–4307.

37 S. Demeshko, G. Leibeling, S. Dechert and F. Meyer, *Dalton Trans.*, 2004, 3782–3787.

38 B. Kozlevcar and P. Segedin, *Croat. Chem. Acta*, 2008, **81**, 369–379.

39 P. Chaudhuri, D. Ventur, K. Wieghardt, E. M. Peters, K. Peters and A. Simon, *Angew. Chem., Int. Ed.*, 1985, **24**, 57–59.

40 H. Buchtelova, Z. Skubalova, V. Strmiska, P. Michalek, S. Kociova, K. Smerkova, R. Kruszynski, A. Bieńko, M. Kaj, A. Lewinska, D. Bieńko, M. Malik-Gajewska, V. Milosavljevic, P. Kopel, Z. Heger and V. Adam, *J. Inorg. Biochem.*, 2019, **191**, 8–20.

41 D. Reta and N. F. Chilton, *Phys. Chem. Chem. Phys.*, 2019, **21**, 23567–23575.

42 J. M. Frost, K. L. M. Harriman and M. Murugesu, *Chem. Sci.*, 2016, **7**, 2470–2491.

43 H. H. Cui, W. Lv, W. Tong, X. T. Chen and Z. L. Xue, *Eur. J. Inorg. Chem.*, 2019, **2019**, 4653–4659.

44 R. Boča, C. Rajnák, J. Titiš and D. Valigura, *Inorg. Chem.*, 2017, **56**, 1478–1482.

45 D. Valigura, C. Rajnák, J. Titiš, J. Moncol, R. Boča and A. Bieńko, *Dalton Trans.*, 2022, **51**, 5612–5616.

46 F. Neese, *Wiley Interdiscip. Rev.:Comput. Mol. Sci.*, 2022, **12**, e1606.

47 F. Weigend and R. Ahlrichs, *Phys. Chem. Chem. Phys.*, 2005, **7**, 3297–3305.

48 C. Adamo and V. Barone, *J. Chem. Phys.*, 1999, **110**, 6158–6170.

49 J. J. Zheng, X. F. Xu and D. G. Truhlar, *Theor. Chem. Acc.*, 2011, **128**, 295–305.

50 S. K. Singh, M. Atanasov and F. Neese, *J. Chem. Theor. Comput.*, 2018, **14**, 4662–4677.

51 E. A. Buvaylo, V. N. Kokozay, O. Y. Vassilyeva, B. W. Skelton, J. Jezierska, L. C. Brunel and A. Ozarowski, *Chem. Commun.*, 2005, 4976–4978.

52 F. Neese, *J. Phys. Chem. Solids*, 2004, **65**, 781–785.

53 L. Noodleman and E. R. Davidson, *Chem. Phys.*, 1986, **109**, 131–143.

54 L. Noodleman, *J. Chem. Phys.*, 1981, **74**, 5737–5743.

55 A. D. Becke, *J. Chem. Phys.*, 1993, **98**, 5648–5652.

56 C. T. Lee, W. T. Yang and R. G. Parr, *Phys. Rev. B:Condens. Matter Mater. Phys.*, 1988, **37**, 785–789.

57 R. H. Hertwig and W. Koch, *Chem. Phys. Lett.*, 1997, **268**, 345–351.

58 K. Yamaguchi, F. Jensen, A. Dorigo and K. N. Houk, *Chem. Phys. Lett.*, 1988, **149**, 537–542.

59 A. J. Cohen, P. Mori-Sánchez and W. T. Yang, *Science*, 2008, **321**, 792–794.

60 L. Goerigk, A. Hansen, C. Bauer, S. Ehrlich, A. Najibi and S. Grimme, *Phys. Chem. Chem. Phys.*, 2017, **19**, 32184–32215.

61 O. V. Nesterova, D. S. Nesterov, J. Jezierska, A. J. L. Pombeiro and A. Ozarowski, *Inorg. Chem.*, 2018, **57**, 12384–12397.

62 Y. Zhao and D. G. Truhlar, *Theor. Chem. Acc.*, 2008, **120**, 215–241.

63 V. N. Staroverov, G. E. Scuseria, J. M. Tao and J. P. Perdew, *J. Chem. Phys.*, 2003, **119**, 12129–12137.

64 J. M. Tao, J. P. Perdew, V. N. Staroverov and G. E. Scuseria, *Phys. Rev. Lett.*, 2003, **91**, 146401.

65 J. W. Furness, A. D. Kaplan, J. L. Ning, J. P. Perdew and J. W. Sun, *J. Phys. Chem. Lett.*, 2020, **11**, 8208–8215.

66 N. Mardirossian and M. Head-Gordon, *J. Chem. Phys.*, 2016, **144**, 214110.

67 A. Najibi and L. Goerigk, *J. Comput. Chem.*, 2020, **41**, 2562–2572.

68 D. Rappoport and F. Furche, *J. Chem. Phys.*, 2010, **133**, 134105.

69 G. Singh, S. Gamboa, M. Orio, D. A. Pantazis and M. Roemelt, *Theor. Chem. Acc.*, 2021, **140**, 139.

70 D. A. Pantazis, *Inorganics*, 2019, **7**, 57.

71 I. F. M. Costa, C. H. J. Franco, D. S. Nesterov, V. André, L. C. J. Pereira and A. M. Kirillov, *J. Phys. Chem. C*, 2024, **128**, 6053–6064.

72 D. S. Nesterov, J. Jezierska, O. V. Nesterova, A. J. L. Pombeiro and A. Ozarowski, *Chem. Commun.*, 2014, **50**, 3431–3434.

73 Z. X. Tian, A. Fattahi, L. Lis and S. R. Kass, *J. Am. Chem. Soc.*, 2006, **128**, 17087–17092.

74 U. Schuchardt, D. Cardoso, R. Sercheli, R. Pereira, R. S. de Cruz, M. C. Guerreiro, D. Mandelli, E. V. Spinace and E. L. Fires, *Appl. Catal., A*, 2001, **211**, 1–17.

75 G. B. Shul'pin, Y. N. Kozlov, L. S. Shul'pina, A. R. Kudinov and D. Mandelli, *Inorg. Chem.*, 2009, **48**, 10480–10482.

76 Y. N. Kozlov, G. V. Nizova and G. B. Shul'pin, *Russ. J. Phys. Chem.*, 2001, **75**, 770–774.

77 I. Gryca, K. Czerwinska, B. Machura, A. Chrobok, L. S. Shul'pina, M. L. Kuznetsov, D. S. Nesterov, Y. N. Kozlov, A. J. L. Pombeiro, I. A. Varyan and G. B. Shul'pin, *Inorg. Chem.*, 2018, **57**, 1824–1839.

78 G. B. Shul'pin, *J. Mol. Catal. A: Chem.*, 2002, **189**, 39–66.

79 M. M. Vinogradov, Y. N. Kozlov, A. N. Bilyachenko, D. S. Nesterov, L. S. Shul'pina, Y. V. Zubavichus, A. J. L. Pombeiro, M. M. Levitsky, A. I. Yalymov and G. B. Shul'pin, *New J. Chem.*, 2015, **39**, 187–199.

80 A. I. Hanopolskyi, V. A. Smaliak, A. I. Novichkov and S. N. Semenov, *ChemSystemsChem*, 2021, **3**, e2000026.

81 S. L. Faber, N. I. Dilmen and S. Becker, *Chemistry*, 2023, **5**, 1288–1301.

82 T. H. Dunning, *J. Chem. Phys.*, 1989, **90**, 1007–1023.

83 D. E. Woon and T. H. Dunning, *J. Chem. Phys.*, 1993, **98**, 1358–1371.

84 N. B. Balabanov and K. A. Peterson, *J. Chem. Phys.*, 2005, **123**, 064107.

85 N. B. Balabanov and K. A. Peterson, *J. Chem. Phys.*, 2006, **125**, 074110.

86 K. A. Peterson and C. Puzzarini, *Theor. Chem. Acc.*, 2005, **114**, 283–296.

87 A. D. Laurent and D. Jacquemin, *Int. J. Quantum Chem.*, 2013, **113**, 2019–2039.

88 J. S. Liang, X. T. Feng, D. Hait and M. Head-Gordon, *J. Chem. Theor. Comput.*, 2022, **18**, 3460–3473.

89 G. Izzet, X. Zeng, D. Over, B. Douziech, J. Zeitouny, M. Giorgi, I. Jabin, Y. Le Mest and O. Reinaud, *Inorg. Chem.*, 2007, **46**, 375–377.

90 H. Yang, J. Du, C. L. Wang and S. Z. Zhan, *Inorg. Chem. Commun.*, 2021, **130**, 108719.

91 M. Meunier, N. Quirke and D. Binesti, *Mol. Simul.*, 1999, **23**, 109–125.

92 M. Langerman, M. van Dorth and D. G. H. Hetterscheid, *Eur. J. Inorg. Chem.*, 2023, **26**, e202300218.